ELSEVIER

Medical Image Analysis 6 (2002) 163–179

MEDICAL IMAGE ANALYSIS

www.elsevier.com/locate/media

Automatic detection and segmentation of evolving processes in 3D medical images: Application to multiple sclerosis

David Rey[a,*], Gérard Subsol[b], Hervé Delingette[a], Nicholas Ayache[a]

[a]*Projet Epidaure, INRIA, 2004 rte des Lucioles, BP93, 06902 Sophia Antipolis Cedex, France*
[b]*LIA-CERI, 339 ch. des Meinajariès, BP1228, 84911 Avignon Cedex 9, France*

Received 2 November 2000; received in revised form 1 July 2001; accepted 26 September 2001

Abstract

The study of temporal series of medical images can be helpful for physicians to perform pertinent diagnoses and to help them in the follow-up of a patient: in some diseases, lesions, tumors or anatomical structures vary over time in size, position, composition, etc., either because of a natural pathological process or under the effect of a drug or a therapy. It is a laborious and subjective task to visually and manually analyze such images. Thus the objective of this work was to automatically detect regions with apparent local volume variation with a vector field operator applied to the local displacement field obtained after a non-rigid registration between two successive temporal images. On the other hand, quantitative measurements, such as the volume variation of lesions or segmentation of evolving lesions, are important. By studying the information of apparent shrinking areas in the direct and reverse displacement fields between images, we are able to segment evolving lesions. Then we propose a method to segment lesions in a whole temporal series of images. In this article we apply this approach to automatically detect and segment multiple sclerosis lesions that evolve in time series of MRI scans of the brain. At this stage, we have only applied the approach to a few experimental cases to demonstrate its potential. A clinical validation remains to be done, which will require important additional work.

Keywords: 3D medical imaging; Automatic detection and segmentation; Evolving processes; Vector field analysis; Vector field operator; Multiple sclerosis

1. Introduction

1.1. Multiple sclerosis data

Multiple sclerosis is a progressive disease with lesions evolving over time. Lesions appear in the central nervous system: encephalon, especially the white matter, spinal cord and optic nerves. Usually lesions are due to a demyelinization with a replacement of cerebro-spinal fluid instead of myelin. There is a natural process of healing: a typical lesion expands to a maximum and then shrinks thanks to remyelinization. Unfortunately, this healing process is limited and rarefies over time. MRI scans make it possible to confirm the diagnosis at the beginning of multiple sclerosis: hypersignals in T2-weighted or proton density images show lesions but do not differentiate edema, demyelinization, sclerosis and eventually necrosis; T1-weighted images show necrosis, and T1 images with gadolinium injections show active demyelinizing areas. Moreover, Guttmann et al. (1999) showed that MRI scans also make it possible to follow-up a patient with multiple sclerosis. In this case a time series of 3D images of a patient is usually acquired from the same modality and with a specific protocol to have similar properties: similar histogram, field of view, voxel size, image size, etc. In this paper we use two sets of multiple sclerosis time series: a proton density and a T2-weighted set of MRI scans. These two time series come from the Brigham and Women's Hospital[1] and from the BIOMORPH European project[2]. The data from the Brigham and Women's Hospital consist

*Corresponding author.
E-mail address: david.rey@sophia.inria.fr (D. Rey).

[1]Thanks to Dr. Guttmann and Dr. Kikinis.
[2]http://www.cs.unc.edu/_styner/biomorph/biomorph.htmlx.

1361-8415/02/$ – see front matter
PII: S1361-8415(02)00056-7

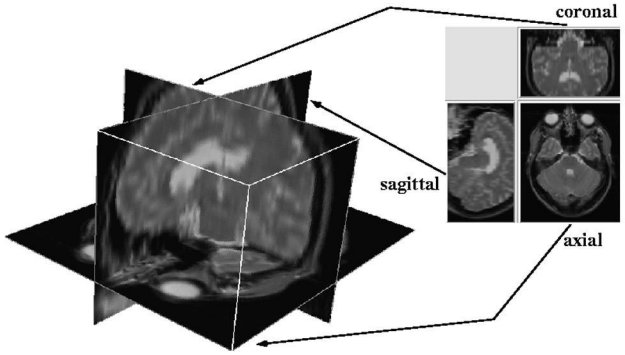

Fig. 1. A 3D image with visualization using InrView freeware.

of 256×256×54 PD images, with a voxel size of 0.9375×0.9375×3.0 mm. There are 24 time points over 1 year with a temporal interval between two images of the series which varies from 1 to 6 weeks with an average of 2 weeks. The data from the BIOMORPH project consist of T2-weighted 256×256×24 images with a voxel size of 0.898438×0.898438×5.5 mm. There are 16 time points over 3 years with a temporal interval between two images of the series of 1 month during the first year, then an examination each 4 months during the second year, and a final examination at the end of the third year.

In this paper we show 3D images with the same views as with our InrView freeware[3] (Fig. 1).

1.2. Detection and segmentation of evolving lesions

In the case of multiple sclerosis, both qualitative and quantitative information is helpful for diagnosis or follow-up. Typical qualitative information is the positions of lesions (or only evolving lesions) either to confirm the pathology (lesions often appear near ventricles) or to correlate them with clinical signs. On the other hand, quantitative information such as total volume of lesions or volume variation of lesions (global or local) is important, for instance to determine if a drug has been efficient for this patient. A segmentation of lesions or evolving lesions gives both qualitative and quantitative information. Because there is a huge amount of data, processing by rater-supervised methods (for instance, manual segmentation) is not very reliable and is too time-consuming, thus precise, reliable and automated methods are needed. Between two examinations, a patient does not have the same position in the acquisition device. Therefore, images at different times are not directly comparable (cf. Fig. 2(a) and (b)). We have to apply a transformation to each image of a series to compensate for the difference in position (translation) and orientation (rotation). This problem of rigid registration is well known and there are many algorithms that give good results in the case of intra-patient and mono-modal alignment (Brown, 1992; Thirion, 1996; Roche et al., 2000; Maes et al., 1997). However, in our case, significant inaccuracy in the alignment can occur:

- an MRI acquisition is usually subject to inhomogeneities, and thus an MR scan is generally spatially biased;
- there is no absolute intensity scale in MRI, thus images are temporally biased;
- there is a partial volume effect in MRI;
- successive slices may be misaligned in MRI due to a motion artifact between interleaved acquisitions;
- there are evolving lesions in our images.

Even with pre-processing of images, the above perturbations can still disturb registration algorithms and in this case there is an inaccuracy in the alignment. After alignment we can compare images, and apply automatic computerized tools to detect and quantify evolving processes

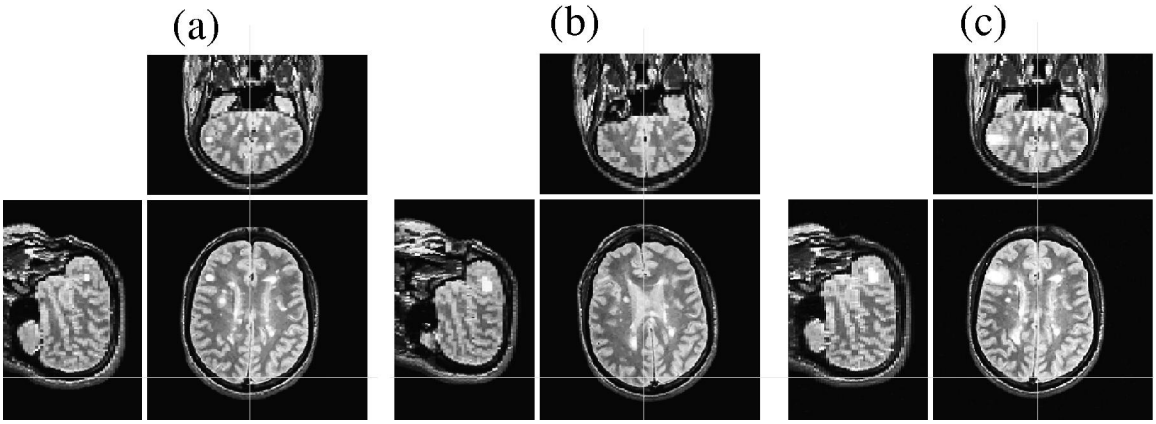

Fig. 2. Two images of a patient at different times are not directly comparable ((a) and (b)), but with a rigid 3D alignment voxels having the same coordinates are comparable ((a) and (c)). We have to apply a transformation to each image of a series to compensate for this difference in position (translation) and orientation (rotation).

[3] http://www-sop.inria.fr/epidaure/Softs/InrView/InrView.html.

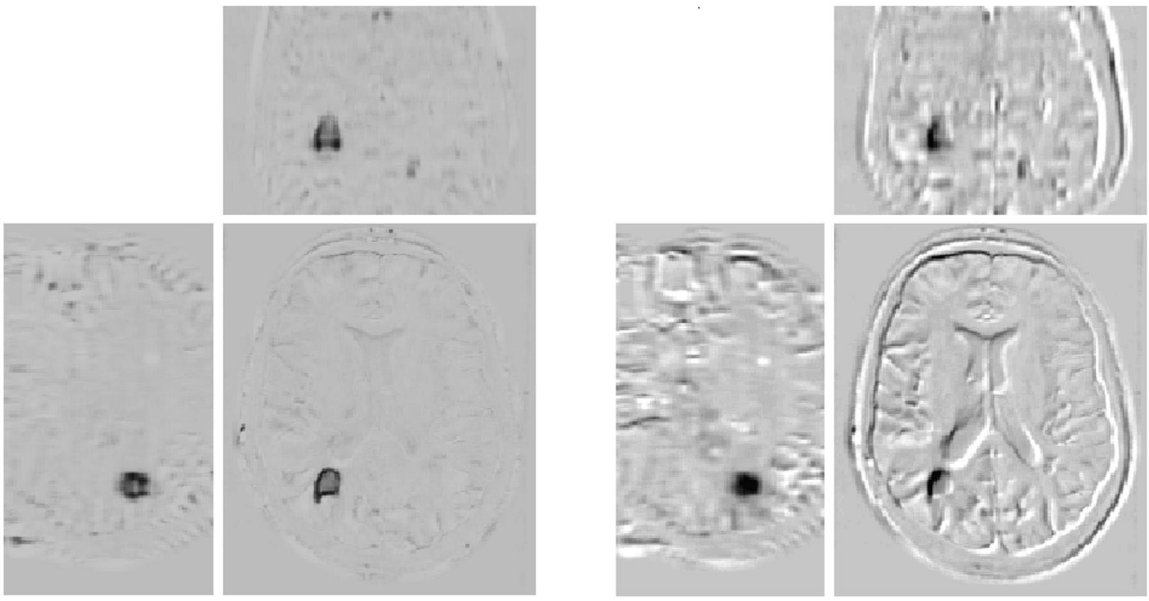

Fig. 3. Comparison between two subtractions with respect to the rigid registration. Left: correct rigid registration: it is easy to detect lesions that evolve (e.g. black hole for a shrinking lesion). Right: approximative rigid registration (this example exaggerates the inaccuracy we obtain with current algorithms): all the anatomical structures appear (e.g. the ventricles, the edges of the brain) and it becomes very hard to distinguish lesions.

(cf. Fig. 2(a) and (c)). There are several automatic methods to study multiple sclerosis lesions in time series:

- With a single image, it is possible to threshold or to study the image intensity to segment lesions independently at each time point (Zijdenbos et al., 1998). Unfortunately, thresholding does not always make it possible to distinguish the lesions from the white matter.
- It is possible to subtract two successive images to find intensity changes. There are two major difficulties when applying such a method. First, the subtraction is dependent on the accuracy of the rigid registration (Hajnal et al., 1995; Lemieux et al., 1998). As explained above, even if the rigid registration process is quite well known, there are difficult cases where alignment is still inaccurate. We show in Fig. 3 an evolving lesion appearing in the subtraction image as a dark hole. But if the images are not perfectly aligned (this example is excessive for emphasis), it is hard to distinguish evolving lesions: the edges of the anatomical structures appear (cortex, ventricles, etc.) and give the same local apparent information as the lesions. Thus it is not trivial to distinguish global rigid changes from local rigid and non-rigid changes. Secondly, the subtraction only characterizes the difference of intensity between two images: there is an intensity difference (a voxel does not have the same intensity in the two images) and a geometrical difference (the same anatomical structures or lesions have different size and/or shape, but the same intensity). The intensities in the subtraction image are not related to the volume/shape evolution of the lesions, but only to the difference between the intensities of lesions and background: we show a synthetic example of this limitation in Fig. 4. If we threshold the subtraction image to automatically extract evolving areas, only some parts of the evolving structures are detected. Moreover, the threshold value is not related to the amplitude of the evolutions, as can be seen in Fig. 4 where a series of threshold values is applied.
- With n images, it is possible to follow the intensity of

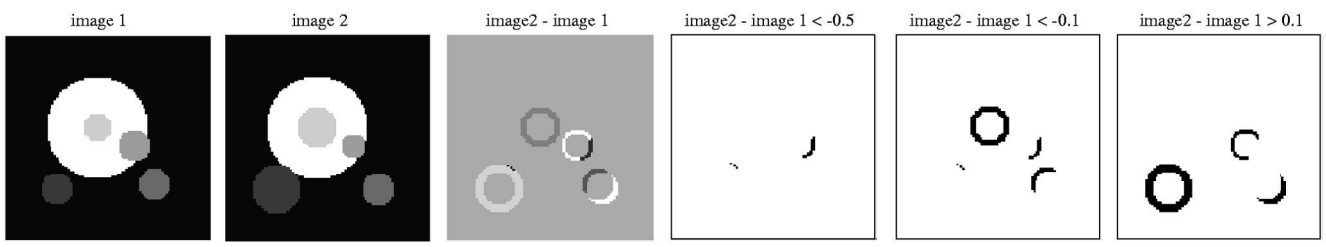

Fig. 4. Different threshold values applied to a subtraction image. For each value, only some parts of the evolving structures are detected. Moreover, the threshold value is not related to the amplitude of the evolutions (volume/shape evolutions).

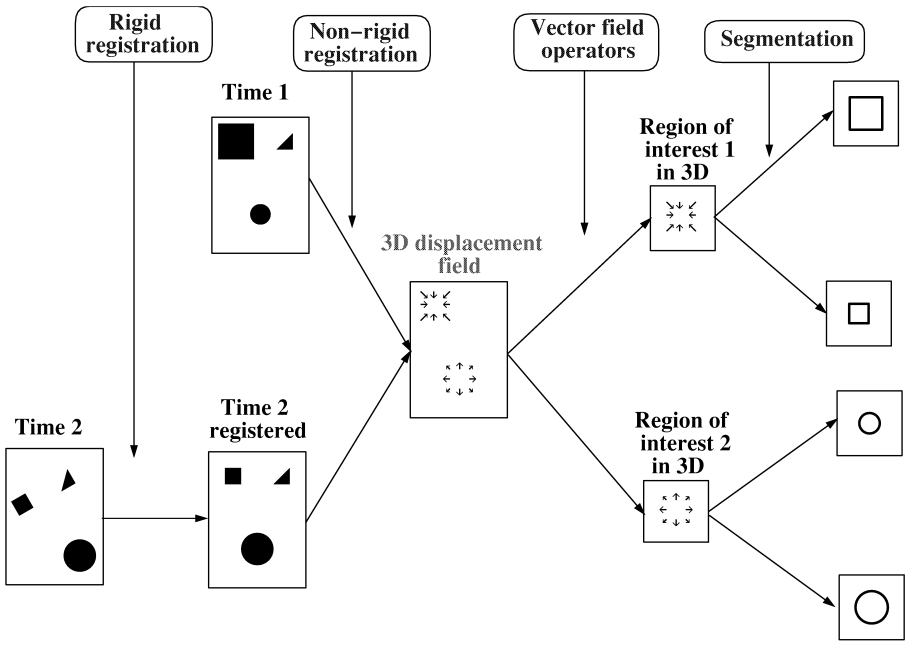

Fig. 5. Method of detection and segmentation of evolving processes using an apparent displacement field computed with a non-rigid registration algorithm.

each voxel over time (Gerig et al., 2000). Although very nice results are obtained with perfectly rigidly aligned images, such an approach remains sensitive to the accuracy of the rigid registration (note that it can be a problem in a very few cases as explained above), and does not take into account the spatial correlation between neighboring voxels. Recently, Welti et al. (2001) proposed the application of a post-treatment to take into account the spatial coherence.

1.3. A new method based on the displacement field

Our idea is to avoid a voxel-by-voxel comparison using the 'apparent' motion between two images. Roughly we want to find a vector at each voxel that expresses its visual motion from one image to another by using a kind of optic flow algorithm (see Section 2.2). Fig. 5 shows the different stages of the automatic process and gives an overview of this paper. First, images are aligned by a rigid registration. Then we compute the displacement field to recover the 'apparent' motion between images with a non-rigid registration algorithm. We focus on the detection of the regions of interest thanks to vector field operators, and use them to segment evolving lesions.

This work is a natural continuation of the previous research work of Thirion and Calmon (1999).

2. Computation of the displacement field

2.1. Rigid registration

First we compute a rigid registration with an algorithm which matches 'extremal' points defined as the maxima of the crest lines of the images (Thirion, 1996). There are several intensity changes between images (especially lesions that evolve), but no global shape differences (intra-patient study); therefore, we preferred a geometrical approach over an intensity-based method to be more robust. Feature points called 'extremal' points are automatically extracted from the 3D image. They are defined as the loci of curvature extrema along the 'crest lines' of the isosurface corresponding to the zero-crossing of the Laplacian of the image. Based on these stable points, a two-step registration algorithm computes a rigid transformation. The first step, called 'prediction', looks for triplets of points from the two sets which can be put into correspondence with respect to their invariant attributes. The second step, called 'verification', checks whether the 3D rigid transformation computed from the two corresponding triplets is valid for all the other points. A study of the accuracy of this algorithm, especially for aligning MS data, can be found in (Pennec and Thirion, 1997).

2.2. Non-rigid registration

We compute a 3D displacement field with a non-rigid algorithm based on local diffusion (Thirion, 1998; Cachier et al., 1999). This algorithm is a kind of optical flow method that diffuses image 2 into image 1. Image 2 is iteratively deformed. At each iteration, each point of image 1 'attracts' or 'repels' the point that has the same coordinates in image 2 according to their intensity difference. All these forces are regularized and used to apply an additional deformation to image 2. The process is iterated based on a multi-resolution scheme. Roughly, this algorithm matches the intensities of two images with a stage of vector field smoothing to avoid large discontinuities and topological

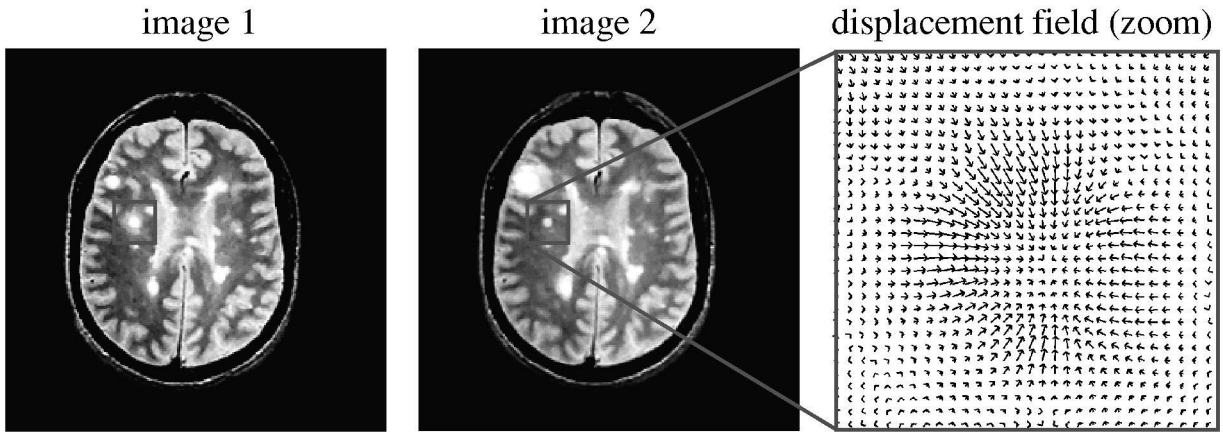

Fig. 6. An example of the computation of the 'apparent' displacement field thanks to a non-rigid registration algorithm. Notice how it emphasizes a shrinking lesion.

problems. If a structure (for instance, a lesion) does not change in shape but changes in intensity (because of the disease or because of the temporal bias) this algorithm interprets such a change as a movement in the center of the given structure. However, contour lines are still well matched because a strong intensity change (step edge) between two structures provides enough contrast for non-linear matching, even if intensities are not equivalent. Thanks to the regularization stage at each iteration of this algorithm, the final resulting vector field does not usually match level sets, but a smooth apparent displacement field is found. Thus the apparent motion in the center of a lesion is influenced by the vectors in the boundary, resulting in a movement towards the center in the case of a shrinking lesion, even if its center intensity changes over time. However, it is possible to avoid this problem by using other algorithms where local intensity differences do not disturb the computation of the apparent displacement vector field as described in (Cachier and Pennec, 2000). In our case we use four multi-resolution levels with four iterations at the highest resolution level and the sigma for the Gaussian smoothing of the vector field is $\sigma = 1.0$.

At the end, each 3D point $P(x,y,z)^{\mathrm{T}}$ of image 1 has a vector $\boldsymbol{u}(u_1(P),u_2(P),u_3(P))$ that gives its apparent *displacement* (cf. Fig. 6). This apparent displacement field informs us where each voxel seems to go visually in image 2. We can also define the *deformation*, which is a function $\phi(\phi_1(P),\phi_2(P),\phi_3(P))$ that transforms the point $P(x,y,z)^{\mathrm{T}}$ into the point $P'(x',y',z')^{\mathrm{T}}$. We thus have

$$\begin{cases} x' = x + u_1(x,y,z) = \phi_1(x,y,z), \\ y' = y + u_2(x,y,z) = \phi_2(x,y,z), \\ z' = z + u_3(x,y,z) = \phi_3(x,y,z). \end{cases}$$

This apparent displacement field $\boldsymbol{u}$ gives an idea of the temporal evolution between two images. We can compute the two fields: from image 1 to image 2, and from image 2 to image 1, which contain complementary information, as we will see in Section 4.1. Fig. 6 shows the vector field from 1 to 2 around a lesion, emphasizing a radial shrinking.

In the next section we introduce a vector field operator in order to transform the 3D vector field into a simpler 3D scalar image. Our objective is to obtain a scalar image enhancing time evolutions. Moreover, we wish to introduce operators that yield scalar values with a physical meaning for a better interpretation of the results.

3. The Jacobian operator

3.1. Mathematical expression and physical meaning

We introduce the Jacobian of the deformation function at point P, as inspired from (Davatzikos et al., 1996): $\phi(\phi_1(P),\phi_2(P),\phi_3(P))$. This operator is widely used in continuum mechanics (Bro-Nielsen, 1997; Weiss et al., 1997). The Jacobian of ϕ at point P is defined as

$$\mathrm{Jac}(\phi) = \det(\nabla_p \phi) = \begin{vmatrix} \frac{\partial \phi_1}{\partial x} & \frac{\partial \phi_1}{\partial y} & \frac{\partial \phi_1}{\partial z} \\ \frac{\partial \phi_2}{\partial x} & \frac{\partial \phi_2}{\partial y} & \frac{\partial \phi_2}{\partial z} \\ \frac{\partial \phi_3}{\partial x} & \frac{\partial \phi_3}{\partial y} & \frac{\partial \phi_3}{\partial z} \end{vmatrix}.$$

It can also be written with the vector displacement field $\boldsymbol{u}(u_1,u_2,u_3)$ at P,

$$\det(\nabla_p \phi) = \det(Id + \nabla_p \boldsymbol{u}) = \begin{vmatrix} \frac{\partial u_1}{\partial x} + 1 & \frac{\partial u_1}{\partial y} & \frac{\partial u_1}{\partial z} \\ \frac{\partial u_2}{\partial x} & \frac{\partial u_2}{\partial y} + 1 & \frac{\partial u_2}{\partial z} \\ \frac{\partial u_3}{\partial x} & \frac{\partial u_3}{\partial y} & \frac{\partial u_3}{\partial z} + 1 \end{vmatrix}.$$

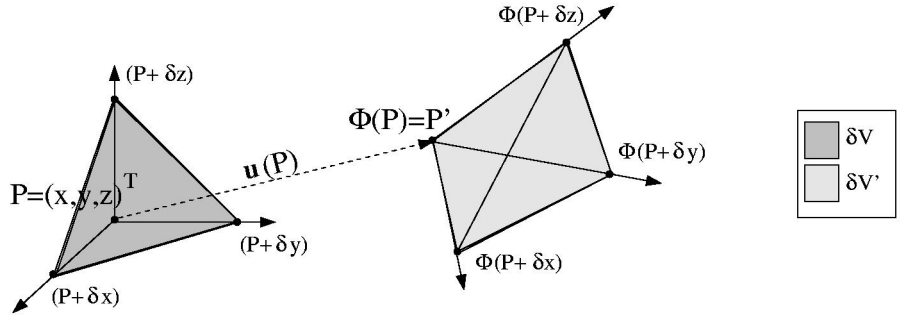

Fig. 7. $\boldsymbol{u}(P)$ is the apparent displacement of P at time 1. $P' = P + \boldsymbol{u}(P)$ is the apparent location of P at time 2. The Jacobian of the apparent deformation measures the local volume variation $\delta V'/\delta V$ (see text).

It is useful to recall a physical interpretation of the Jacobian operator in terms of local volume variation. With the notation of Fig. 7, $\boldsymbol{u}(P)$ is the apparent displacement of P at time 1. $P' = P + \boldsymbol{u}(P)$ is the apparent location of P at time 2. The volume δV of the elementary tetrahedron defined by $(P, P + \delta x, P + \delta y, P + \delta z)$ is given by the determinant of the three vectors from P (triple product),

$$\delta V = \frac{1}{6}\begin{vmatrix} x+\delta x & x & x \\ y & y+\delta y & y \\ z & z & z+\delta z \end{vmatrix}.$$

So,

$$\delta V = \frac{1}{6}\begin{vmatrix} \delta x & 0 & 0 \\ 0 & \delta y & 0 \\ 0 & 0 & \delta z \end{vmatrix}.$$

And, finally,

$$\delta V = \tfrac{1}{6}\delta x \delta y \delta z.$$

As we assume that δx is small, a first-order approximation of the deformation ϕ in P is given by

$$\phi(P + \delta x) = \phi(P) + \frac{\partial \phi}{\partial x}\delta x + \mathrm{o}(\delta x^2).$$

We have the same approximation in the y and z directions. Thus the volume $\delta V'$ of the deformed elementary tetrahedron is

$$\delta V' \simeq \frac{1}{6}\begin{vmatrix} \frac{\partial \phi_1}{\partial x}\delta x & \frac{\partial \phi_1}{\partial y}\delta y & \frac{\partial \phi_1}{\partial z}\delta z \\ \frac{\partial \phi_2}{\partial x}\delta x & \frac{\partial \phi_2}{\partial y}\delta y & \frac{\partial \phi_2}{\partial z}\delta z \\ \frac{\partial \phi_3}{\partial x}\delta x & \frac{\partial \phi_3}{\partial y}\delta y & \frac{\partial \phi_3}{\partial z}\delta z \end{vmatrix} = \frac{1}{6}\mathrm{Jac}_{\mathrm{p}}(\phi)\delta x \delta y \delta z.$$

Therefore,

$$\delta V' \simeq \mathrm{Jac}_{\mathrm{p}}(\phi) \cdot \delta V.$$

Thus, the local variation $\delta V'/\delta V$ of an elementary volume is given (as a first-order approximation) by the Jacobian of the deformation function ϕ. When $\mathrm{Jac}_{\mathrm{p}}(\phi) > 1$ there is a local expansion at point P, and when $\mathrm{Jac}_{\mathrm{p}}(\phi) < 1$ there is a local shrinking at point P. The transformation locally preserves the volume when $\mathrm{Jac}_{\mathrm{p}}(\phi) = 1$.

3.2. Robustness of the Jacobian with respect to misalignment

Fig. 8 shows what happens when two images are not perfectly aligned: the deformation function ψ, which is measured, is different from the ideal one ϕ. The misregistration is given by a residual rotation R and translation t. We have $\psi = R \circ \phi + t$. Then we have

$$\mathrm{Jac}(\psi) = \det(\nabla\psi) = \det(\nabla(R \circ \phi + t)) = \det(R \cdot \nabla\phi).$$

Thus,

$$\mathrm{Jac}(\psi) = \det(R)\det(\nabla\phi) = \det(\nabla\phi) = \mathrm{Jac}(\phi).$$

This shows that the Jacobian is invariant with respect to imperfect rigid registration of the images. Of course, it requires that, even in the case of an approximate alignment of images, the non-rigid registration algorithm still computes a correct displacement field. This is actually the case as long as the original rigid alignment remains close to the ideal one: for the demons algorithm, a multiscale approach implementation makes it possible to recover additional displacement typically up to five voxels. It is therefore much less constrained than when employing the subtraction method where a precision of the initial rigid alignment typically better than one voxel is required.

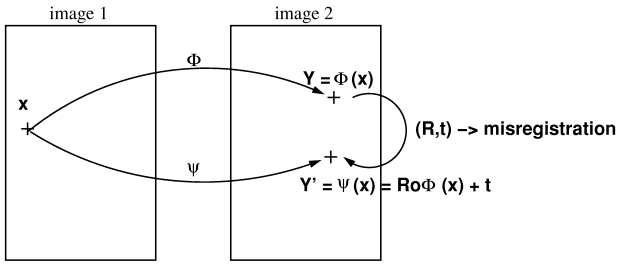

Fig. 8. ϕ is the deformation function for a perfect rigid registration, and ψ is the deformation function when there is a misregistration (R,t). We have $\psi = R \circ \phi + t$.

3.3. Computation and application of the Jacobian

We have seen that the computation of the Jacobian of the deformation ϕ can be performed directly with the displacement field $\boldsymbol{u}$. We need to compute the first nine derivatives of the displacement field $\boldsymbol{u}$,

$$\frac{\partial u_x}{\partial x}, \frac{\partial u_x}{\partial y}, \frac{\partial u_x}{\partial z}, \ldots, \frac{\partial u_z}{\partial z}.$$

For a faster computation we use recursive filtering which gives an image for each derivative. Then, we need to store in memory the 9 derivatives to compute the Jacobian and for an image of $256\times256\times180$; this requires about 425 Mbytes of memory. So, to avoid overfilling the memory space, we compute the Jacobian on sub-images and then we fuse the different sub-results which include an overlapping border to avoid side effects. We have also implemented another method to compute the Jacobian: at each point we calculate an approximation of the vector field by an affine transformation thanks to an affine least square method described in (Pennec, 1996). We have a 3×3 matrix A which corresponds to the linear part of the nearest (in a least-square sense) affine transform and a 3×1 translation vector t at each point $P(x,y,z)$ such that

$$P'(x',y',z') \simeq A\cdot P(x,y,z) + t$$

and

$$\boldsymbol{u} = P'(x',y',z') - P(x,y,z) \simeq A\cdot P + t - P$$
$$= (A - Id)\cdot P + t.$$

So,

$$\mathrm{Jac}_p(\phi) = \det(Id + \nabla_p(\boldsymbol{u}))$$
$$\simeq \det(Id + \nabla_p((A - Id)\cdot P + t)$$
$$= \det(Id + (A - Id)).$$

And, finally, at each point $P(x,y,z)$,

$$\mathrm{Jac}(\phi) \simeq \det(A).$$

It is thus possible to compute a good approximation of the Jacobian at each point by calculating the determinant of the linear part of the approximative local affine transformation. This method gives results very similar to that using recursive filters, and can be faster (about 4 times) when using a very small neighborhood (typically the 6-neighborhood of each voxel) to calculate the nearest affine transform with a least-square estimation.

The Jacobian gives a contrasted image related to the volume variation of each evolving lesion. The most contrasted areas correspond to the most shrinking or most expanding lesions. In Fig. 9 we show the result of the Jacobian operator on a synthetic vector field: this synthetic field deforms a ball to half its size with a linear decrease of the vectors along the radius. In this case, the Jacobian has a constant value smaller than 1 which expresses a shrinking in the middle of the ball; the Jacobian value equals 1 outside the ball where nothing happens; and there is an area with a value greater than 1 because, on the boundaries of the ball, the vectors suddenly pass from 0 to their maximum value, which appears locally as an expansion (in a real case, the field is smoothed and continuous, but, on the boundaries of the lesions, the effect is the same: the vectors outside the lesion are smaller than those just

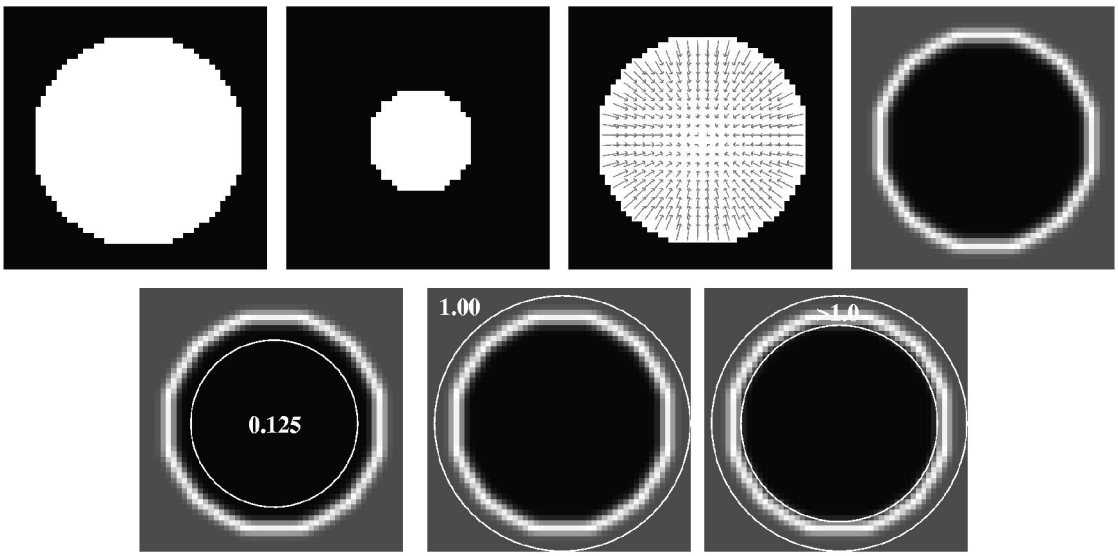

Fig. 9. The synthetic field deforms a ball to half its size with a linear decrease of the vectors along the radius. In this case, the Jacobian has a constant value smaller than 1 which expresses a shrinking in the middle of the ball; the Jacobian value equals 1 outside the ball where nothing happens; and there is an area with a value greater than 1 because the vectors suddenly pass from 0 to their maximum value on the boundaries of the ball: it appears locally as an expansion (in a real case, the field is smoothed and continuous, but on the boundaries of lesions the effect is the same: the vectors outside lesions are smaller than those just inside).

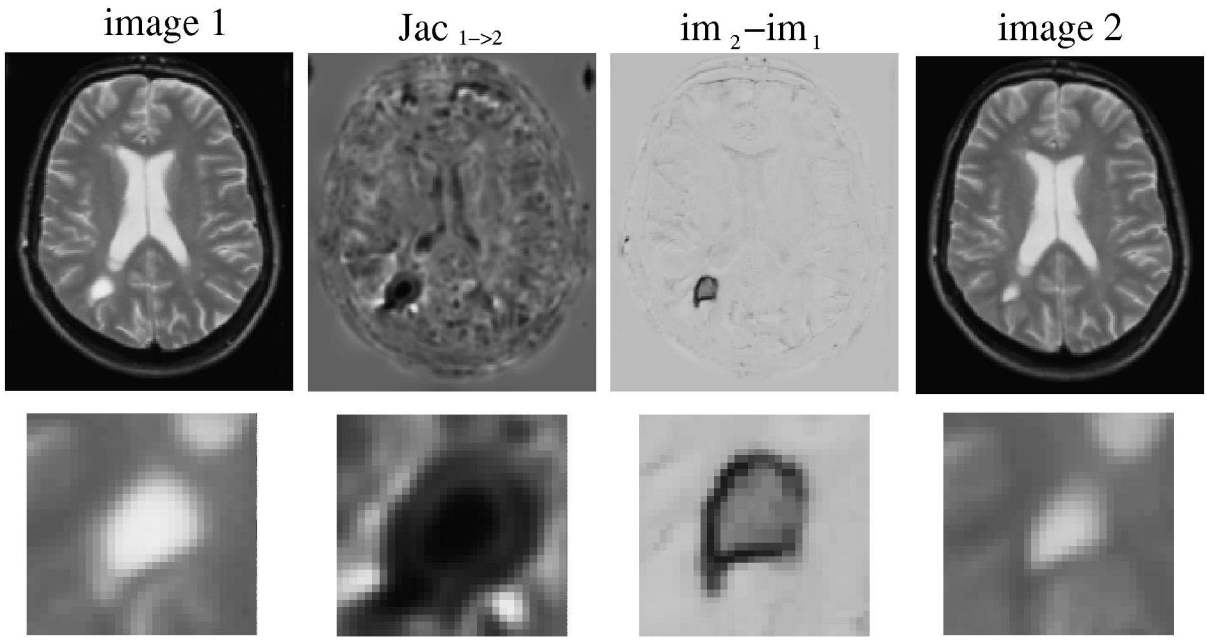

Fig. 10. Application of the Jacobian to a real case: we can see a lesion that shrinks between image 1 and image 2. On the Jacobian from image 1 to image 2 we can see a black hole corresponding to a shrinking area (Jacobian smaller than 1). The subtraction image also shows an evolving voxel, but with a value which is not related to the volume variation.

inside). In Fig. 10 we see that an important shrinking of a lesion between two images gives a dark region in the Jacobian image. In other areas, the value is almost constant and very close to 1, which indicates no apparent variation of volume. Zooming in around a lesion shows that darker areas correspond to shrinking lesions.

3.4. Other operators

Thirion and Calmon (1999) have developed another vector field operator based on the divergence and the norm of the displacement field $\boldsymbol{u}$,

$$\begin{aligned}\text{norm} \cdot \text{div}(P) &= \|\boldsymbol{u}(P)\| \text{div}\, \boldsymbol{u}(P) \\ &= \|\boldsymbol{u}(P)\| \left(\frac{\partial u_1}{\partial x} + \frac{\partial u_2}{\partial y} + \frac{\partial u_3}{\partial z} \right).\end{aligned}$$

This operator has no simple physical meaning even if the sign of the operator gives information about shrinking (negative values) or expansion (positive values). As we have no physical interpretation of the value, it is difficult to automatically threshold the image to extract the regions of interest.

Prima et al. (1998) proposed another operator which gives the local variation of volume. A cell of voxels of volume V_1 is deformed to a complex polyhedron, the volume V_2 of which is computed. Then $(V_2 - V_1)/V_1$ is calculated. Note that another algorithm to compute V_2 is given in (Calmon et al., 1998). This operator is directly related to the Jacobian,

$$\frac{V_2 - V_1}{V_1} = \frac{V_2}{V_1} - 1 \simeq \text{Jac} - 1.$$

Fig. 11 shows the application of these three operators on the same displacement field. In particular, we notice how the Jacobian and the discrete computation of the relative variation of volume are similar. The advantage of our approach is that it provides a continuous framework for a computation of the Jacobian at any scale.

In (Rey et al., 1999) we present other vector field operators based on continuum mechanics, one that gives the deformation energy and another that gives a value of shearing at each voxel. These operators are less convenient than the Jacobian because they do not have a simple reference value, and they do not make it possible to distinguish between expansion and shrinking.

4. Results

4.1. Thresholding and segmentation

We can extract the areas that correspond to a significant temporal evolution. It is possible to find a uniform threshold over the whole Jacobian image relying on its physical interpretation in terms of local variation of volume. We chose an empirical threshold of 0.3 to indicate significant shrinking. The example in Fig. 12 shows that it gives a good segmentation of a shrinking lesion. In fact, we are going to focus only on the shrinking areas. We can see in Fig. 13 that a better description is provided with the

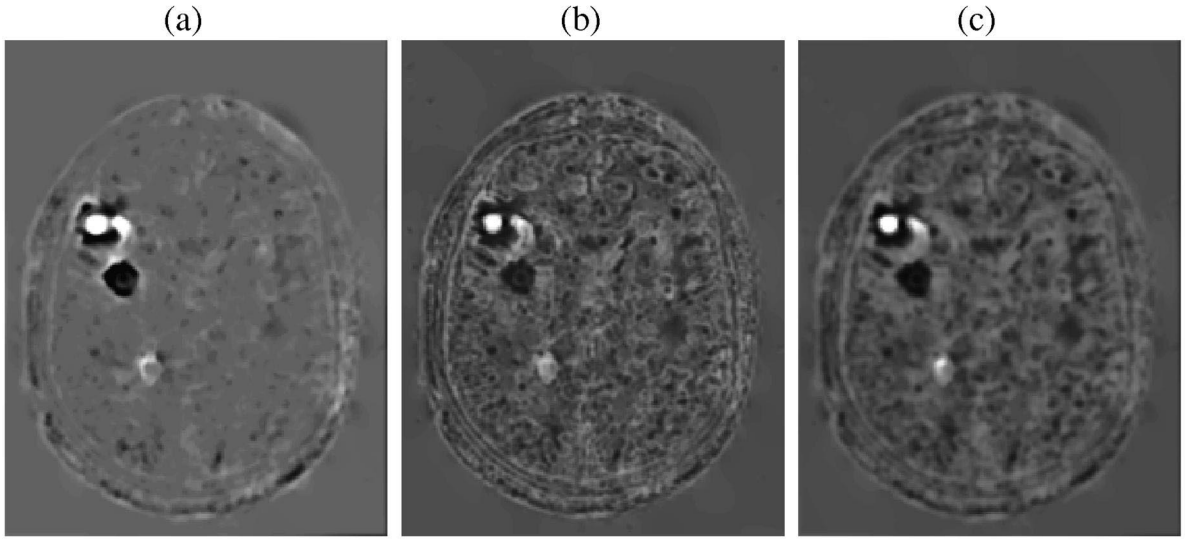

Fig. 11. Comparison between different existing operators: (a) $\|\boldsymbol{u}\|\mathrm{div}\ \boldsymbol{u}$; (b) discrete computation of $(V_2 - V_1)/V_1 \sim (\mathrm{Jac}(\phi) - 1)$; (c) Jacobian.

shrinking field. If there is an expansion locally between images 1 and 2, in most cases we would need a one-to-many mapping due to the limited resolution of the image. Moreover, the smoothing step during the non-rigid registration creates asymmetry between the direct and reverse field because expanding areas are smaller than corresponding shrinking areas and thus are more influence by the spatial smoothing. To avoid this, we consider only shrinking regions from 1 to 2, and then shrinking regions from 2 to 1. By thresholding shrinking areas we obtain the segmentations $s_{1\to 2}$ in the first image, and $s_{2\to 1}$ in the second image. Then we have to combine these two sources of information: the whole segmentations in images 1 and 2 are given by

$$S_{12}(t1) = [s_{1\to 2}] \cup [\boldsymbol{u}_{2\to 1}(s_{2\to 1})]$$

and

$$S_{12}(t2) = [s_{2\to 1}] \cup [\boldsymbol{u}_{1\to 2}(s_{1\to 2})].$$

Figs. 14–16 show automatic segmentation results obtained

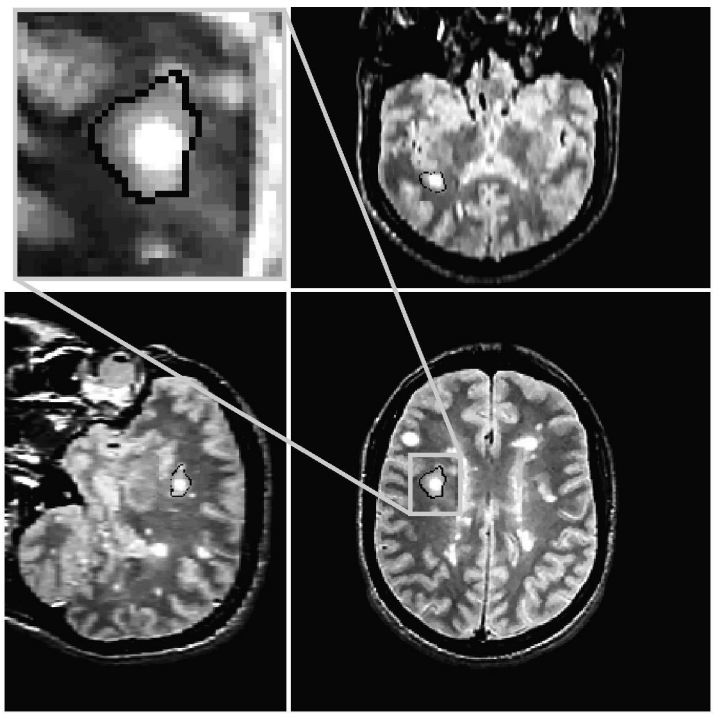

Fig. 12. The threshold $\det(\nabla\phi) < 0.3$ makes it possible to segment shrinking lesions. This example is for a region of interest around a lesion but we show it in the complete image to locate the lesion.

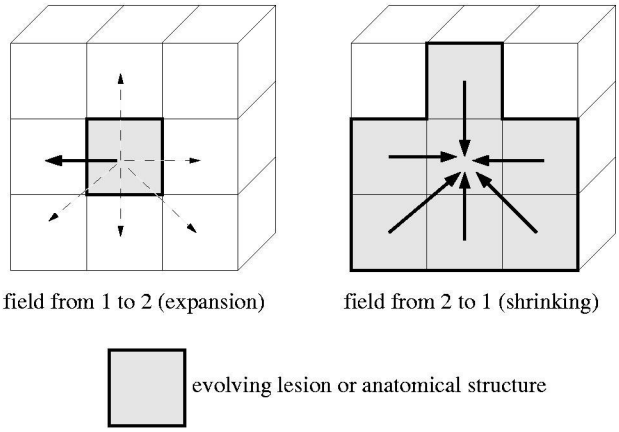

Fig. 13. The information is richer when we look at the shrinking field. Left: If there is a large expansion, the direct displacement field cannot express that one voxel should deform to several voxels. We would need a one-to-many mapping due to the limited resolution of the image. Right: Thanks to the reverse field, a better description of the phenomenon is possible. Moreover, the smoothing step during the non-rigid registration creates asymmetry between the direct and reverse field because expanding areas are smaller than the corresponding shrinking areas and thus are more influenced by the spatial smoothing.

at two time points. We have recently developed a simpler method that uses a quasi-symmetrical vector field computation to have a symmetrical value to directly threshold expanding and shrinking areas with only one vector field (Cachier and Rey, 2000).

With the fields between images 1 and 2 and between images 2 and 3, we can compute segmentations S_{12} in images 1 and 2 and S_{23} in images 2 and 3. Then we propagate the segmentations S_{12} and S_{23}, respectively, to times $t3$ and $t1$, thanks to the vector fields $\boldsymbol{u}_{21}$ and $\boldsymbol{u}_{23}$. Then, by addition, we obtain a segmentation of the lesions in all the images of a series (Rey et al., 1998). In Fig. 17, we can see the results of the method for three time points of the BIOMORPH data set.

4.2. Study of a synthetic example

We have created two images, I_1 and I_2, by including two evolving artificial 3D lesions into the same 3D T2-weighted image of a brain without lesions. The artificial lesions are represented by spheres of radius 10 and 4 mm for I_1, and 6 and 8 mm for I_2 (Fig. 19(a)). Even if the model is extremely simple, with this example we aim to show the feasibility of the method and its limitations. Because the global rigid registration of I_1 and I_2 is the identity in this case, we have only applied the non-rigid registration algorithm to compute the direct and reverse local displacement field everywhere. We then applied our method to extract the boundary of the evolving regions, with $\mathrm{Jac}(\phi) < 0.3$. The results in Figs. 18 and 19(c) show that the evolving regions are correctly detected. The accuracy of the delimitation of the boundary is qualitatively correct, but we observed a difference of between 5 and 20% between the correct diameter of the lesions and the measured diameter.

4.3. Refinement of the segmentation

We have demonstrated that the method makes it possible to accurately detect the evolving areas and that the segmentation is approximate, even for a synthetic example. We used a method based on deformable models (Montagnat and Delingette, 1998) to refine the segmentation of the evolving lesions. This deformable model has the advantage of combining both geometric and image information to perform image segmentation. Indeed, a deformable model evolves under the influence of internal and external forces: internal forces enforce the geometric regularity of the surface model, whereas external forces push the surface towards the lesion boundary through the use of the image gradient information. This method gives a better segmentation of the evolving lesions and makes it possible to perform quantitative measurements of the evolving areas (volume variation, etc.) (cf. Fig. 20).

4.4. Validation

Studying a synthetic example does not consist of a

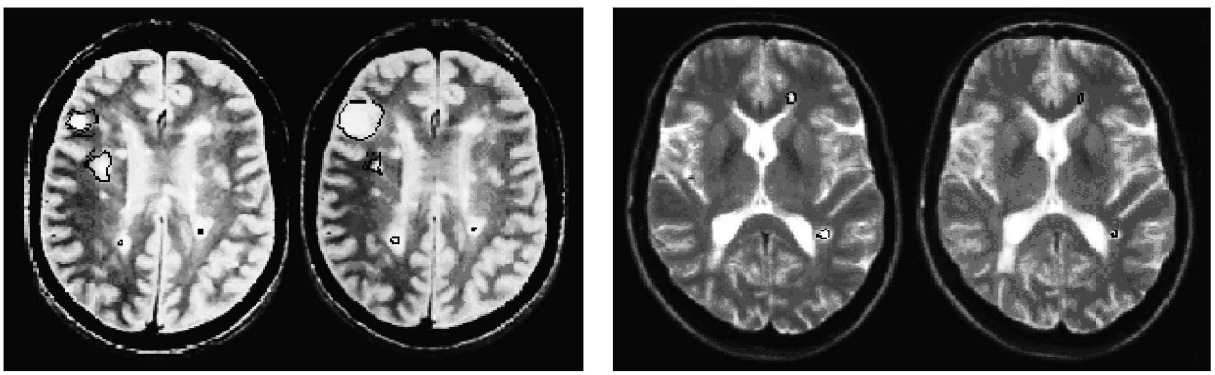

Fig. 14. Segmentation of evolving lesions. Left: Brigham & Women's Hospital data. Right: BIOMORPH data.

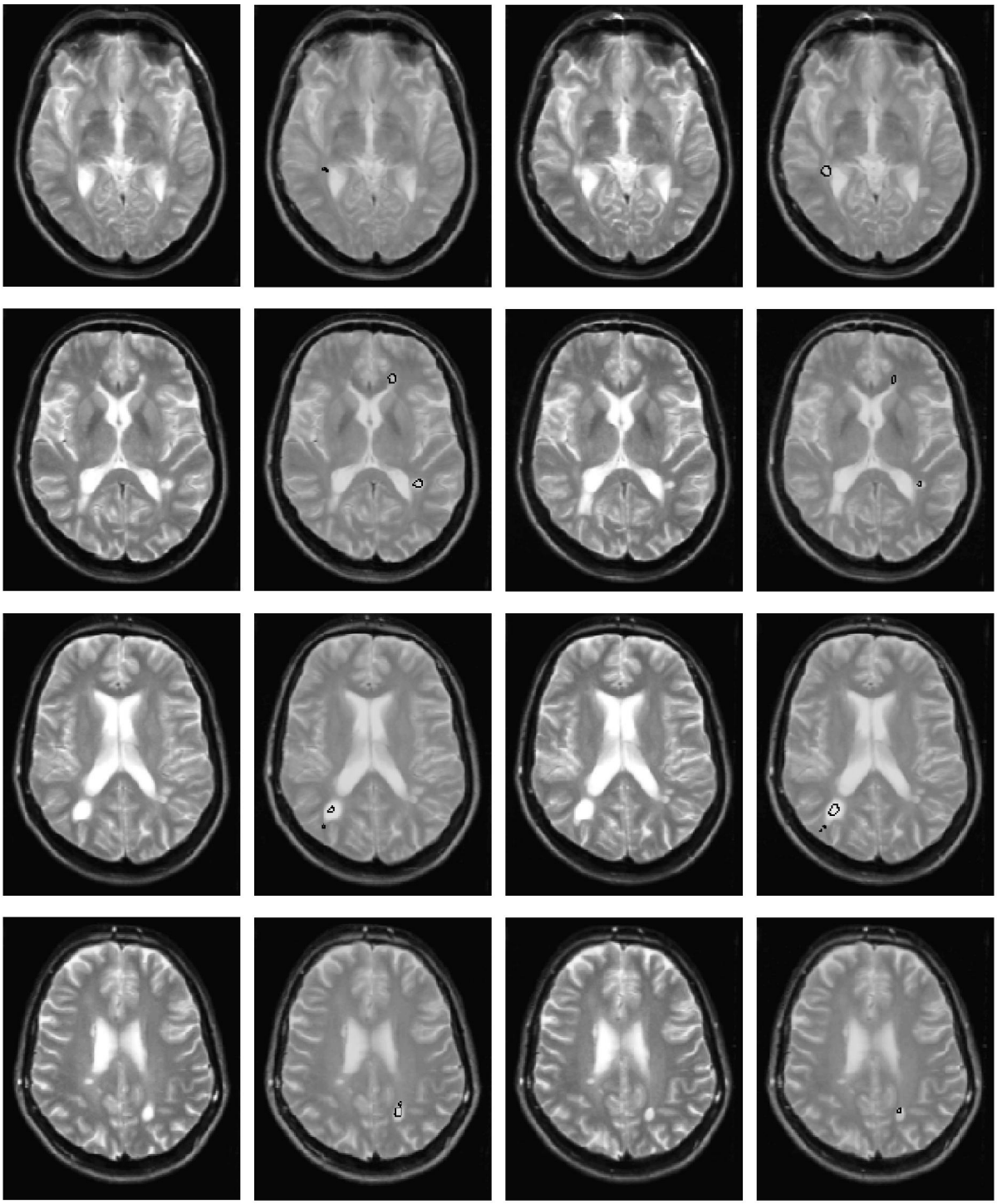

Fig. 15. Segmentation of evolving lesions between two time points of the BIOMORPH data set. On each line we show the result on a different slice. First column: image at time 1. Second column: image at time 1 with segmentation. Third column: image at time 2. Fourth column: image at time 2 with segmentation.

clinical validation; it just shows that our algorithm works properly. A real validation is much more complicated to achieve. We have begun to work in collaboration with the Departments of Neurology (Pr. Chatel and Dr. Lebrun-Frénay) and Radiology (Dr. Chanalet) of the CHU (Hospital and University Center), Nice, to correlate the results of our method, which detects and segments evolving lesions, with the clinical aspects of multiple sclerosis. This validation will require a long period of time (about 2 years) and the results will be published in a forthcoming paper. Some preliminary results have been presented in (Rey et al., 2000; Lebrun-Frénay et al., 2000).

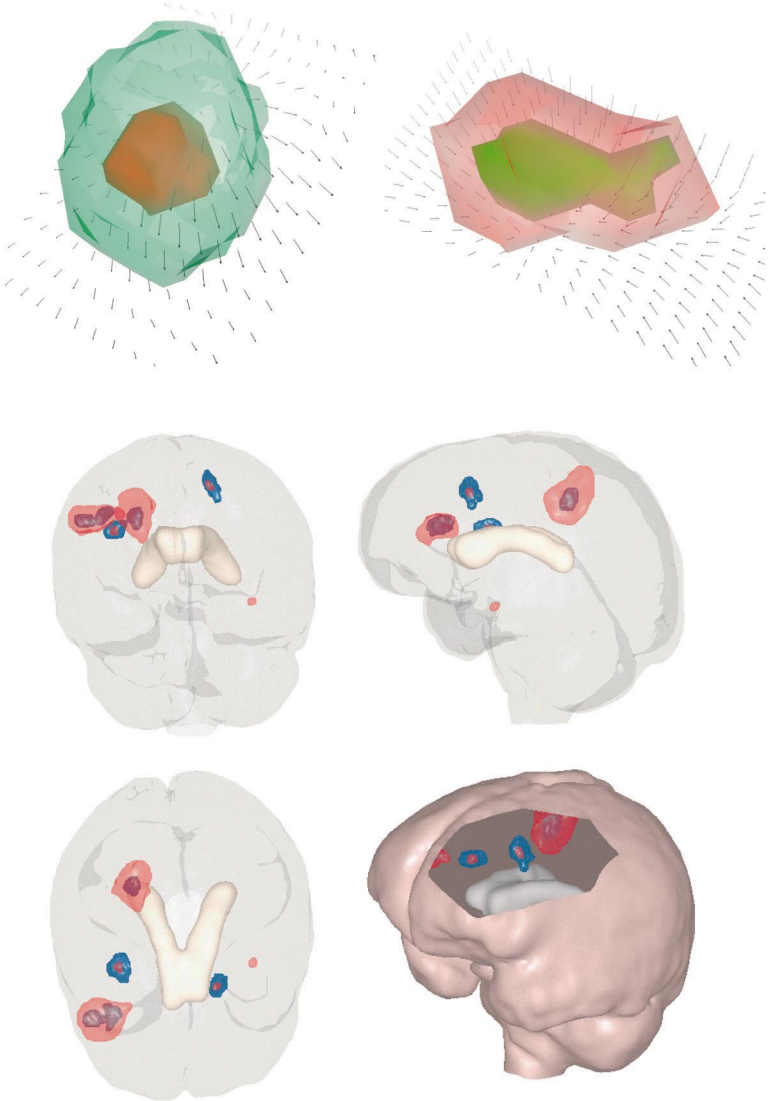

Fig. 16. 3D views of the segmentation of evolving lesions between two time points. Top: A shrinking and an expanding lesion (red corresponds to the lesions at the first time point and green at the second time point). Bottom: Whole brain in 3D with segmented evolving lesions (blue corresponds to the first time point, red to the second time point).

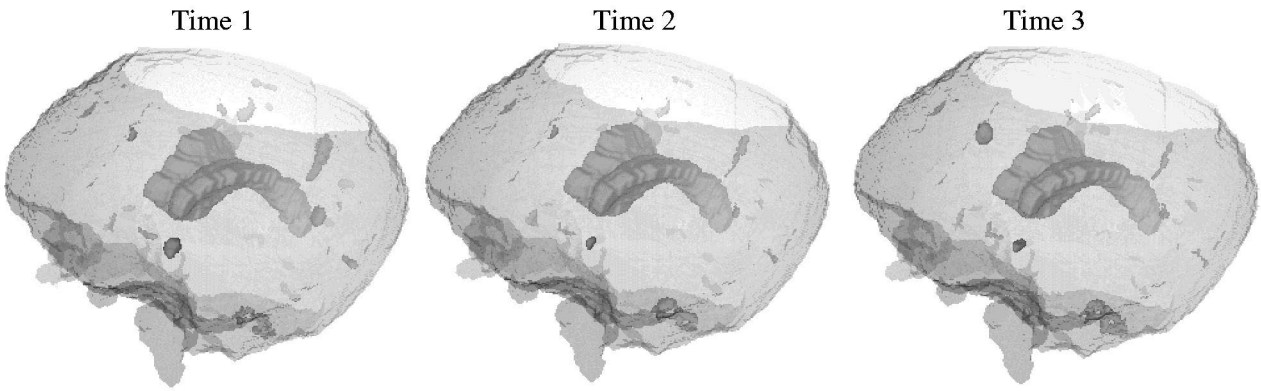

Fig. 17. Thanks to the segmentation of the evolutions between times 1 and 2, and between times 2 and 3, it is possible to visualize lesion evolution between the 3 successive acquisitions.

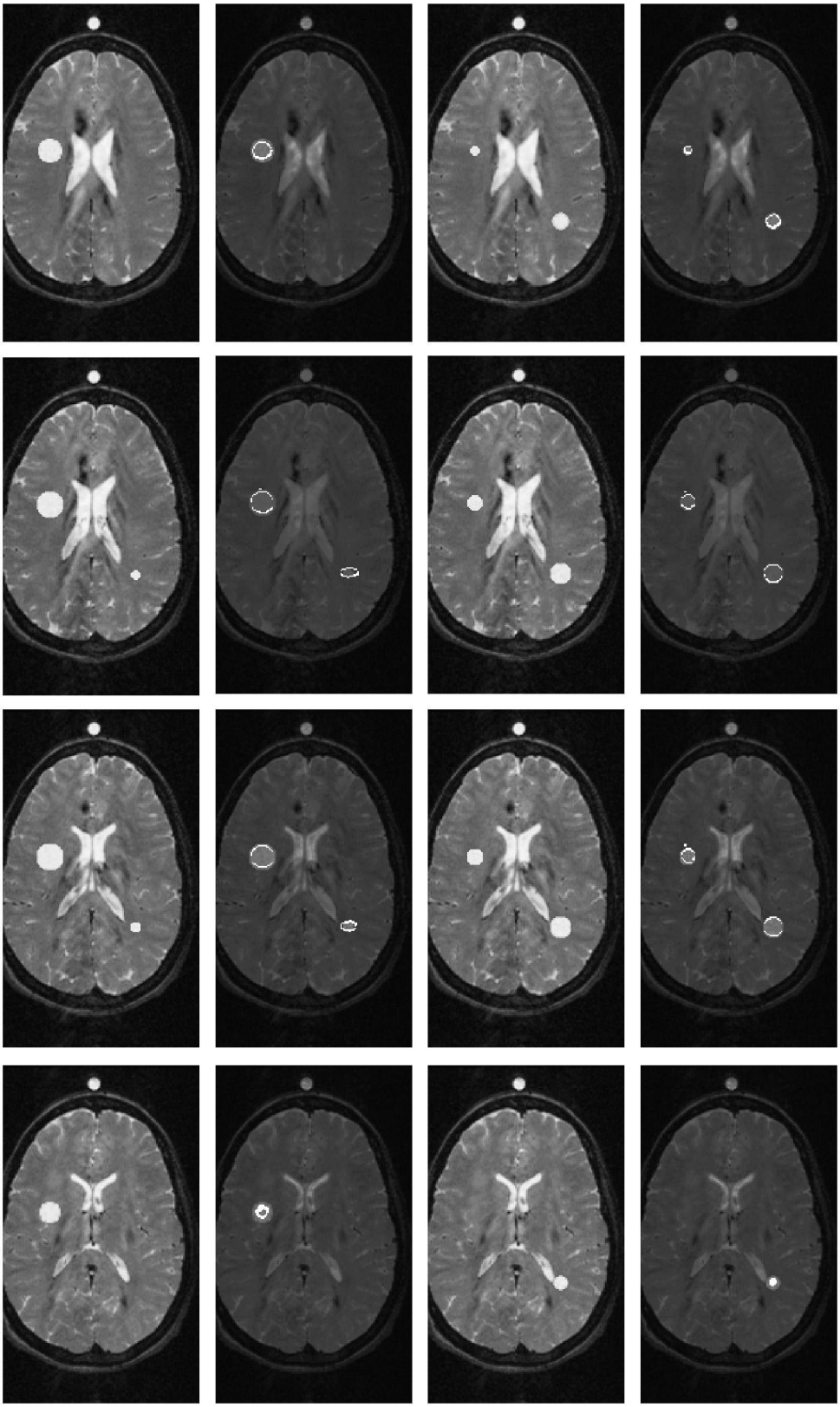

Fig. 18. Results for several 2D slices: each row corresponds to a different slice; the first column represents image 1 without segmentation, the second column shows image 1 with automatic segmentation, the third column represents image 2 without segmentation, and finally the fourth column shows image 2 with segmentation.

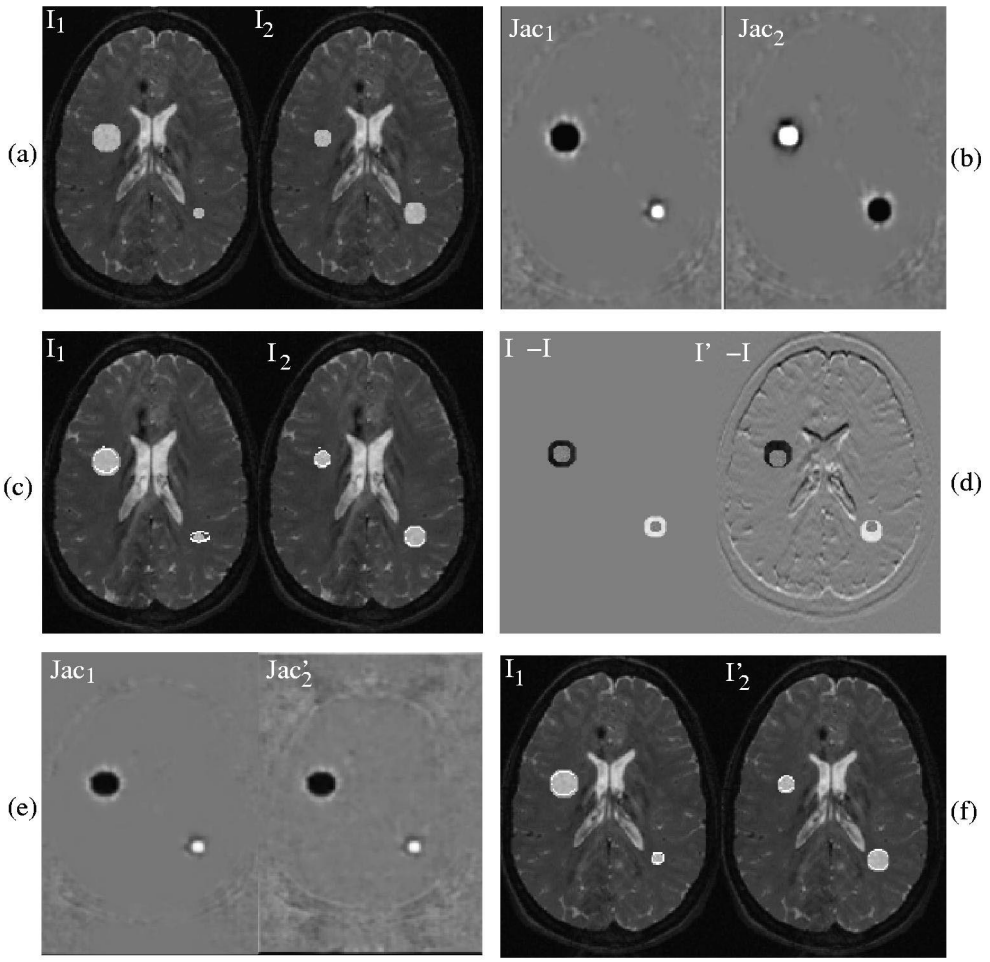

Fig. 19. (a) Two synthetic temporal images I_1 and I_2. (b) The Jacobian image of the field from I_1 to I_2 and I_2 to I_1. (c) Automatic segmentation of evolving lesions in I_1 and I_2 using $\mathrm{Jac}(\phi) < 0.3$. (d) $I_2 - I_1$ on the left. On the right $I_2' - I_1$, where I_2' is a translated version of I_2. (e) Comparison between the Jacobian from I_1 to I_2 and the Jacobian from I_1 to I_2'; evolving areas clearly appear in the two images. (f) Automatic segmentation of evolving lesions in I_1 and I_2' using the Jacobian from I_1 to I_2', which shows robustness to imperfect rigid registration of images.

4.5. Robustness with respect to imperfect rigid registration

From the previous example, we also created an image I_2' by translating I_2 by 3 voxels in one direction. As expected, our method provides similar results when applied to I_1 and I_2' (Fig. 19(e)), while a simple difference yields very noisy results (Fig. 19(d)).

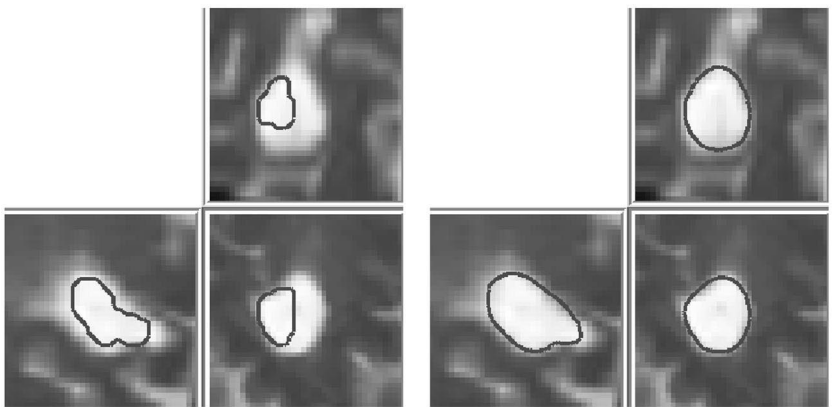

Fig. 20. Refinement of the initial segmentation. Left: Three projections of the segmentation of a 3D evolving lesion. Right: The same lesion with its segmentation refined by deformable models.

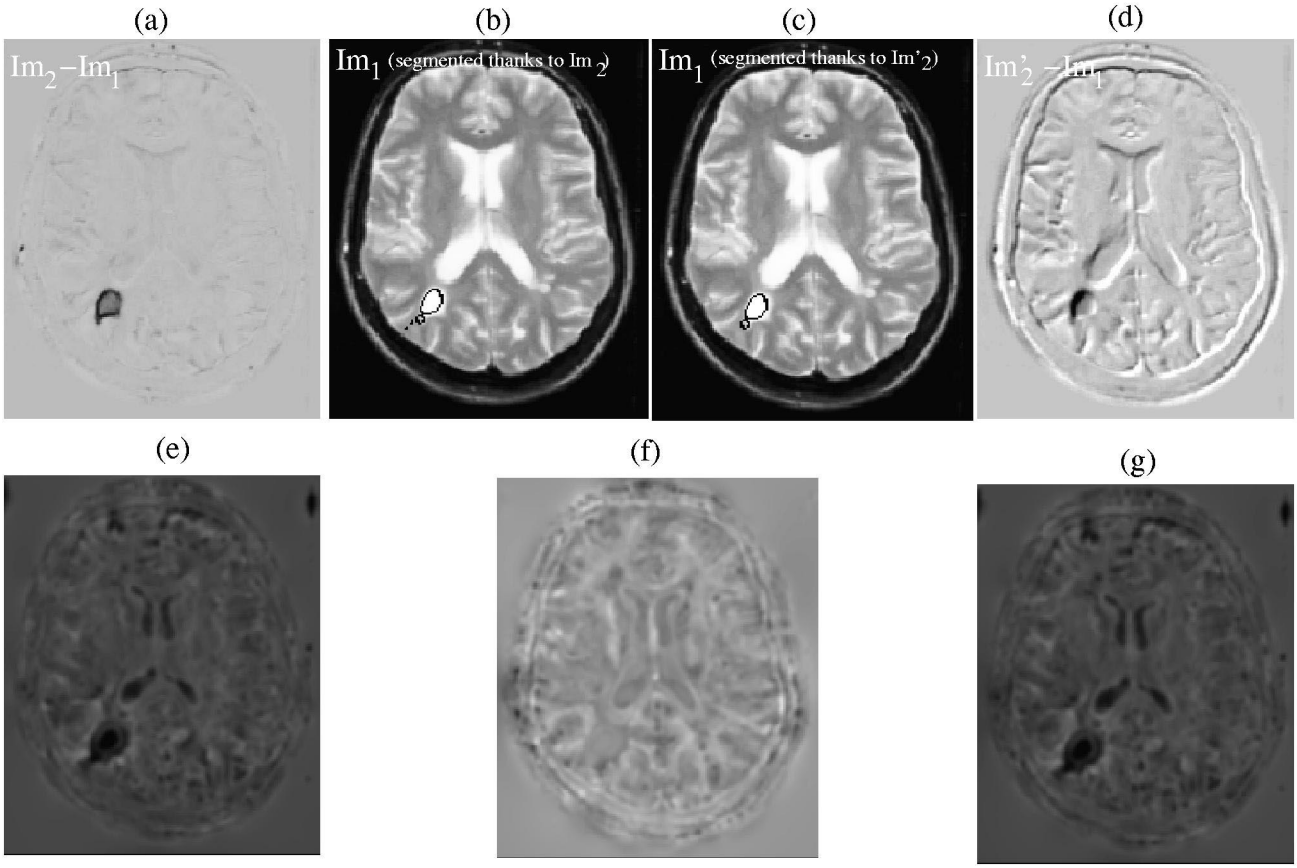

Fig. 21. Segmentation of evolving lesions in Im_1 thanks to a study between Im_1 and Im_2 of Fig. 10 (perfectly rigidly registered) and between Im_1 and Im_2', where Im_2' is a misregistered version of Im_2. This study shows the robustness with respect to imperfect rigid registration. (a) $Im_2 - Im_1$. (b) Automatic segmentation in Im_1 thanks to a study between Im_1 and Im_2. (c) Automatic segmentation in Im_1 thanks to a study between Im_1 and Im_2'. (d) $Im_2' - Im_1$. (e) Jacobian from Im_1 to Im_2. (f) Subtraction between (g) and (e); the maximum difference value is about 25% of the Jacobian maximum value, and the mean difference value is about 6% of the mean Jacobian value. (g) Jacobian from Im_1 to Im_2.

We also considered the application of our method between two real T2-weighted MR images, Im_1 and Im_2 (same 3D images as presented in Fig. 6). When Im_1 and Im_2 are perfectly rigidly registered, our method produces the segmentation of an evolving lesion in cross-section (Fig. 21(b)), which can be compared to a simple difference analysis between the registered images (Fig. 21(a)). We also created an image Im_2' by adding a misalignment to I_2 corresponding to a rotation of 1° around an axis orthogonal to this cross-section and passing through its center, plus a translation of one voxel in the two directions of the plane of this cross-section. We observe that the results provided by our method (Fig. 21(c)) remain similar to the results of Fig. 21(b), whereas a simple difference now produces very noisy results (Fig. 21(d)).

5. Conclusion

In this article we have proposed a new method to study multiple sclerosis lesion evolution over time based on the apparent displacement field between two images. We believe that our approach will be useful to detect evolving regions corresponding to local apparent expansion or shrinking. At this stage, we have only applied the approach to a few experimental cases to demonstrate its potential: the method gives satisfying results for the detection of evolving areas and especially evolving lesions (and has the advantage of not being very dependent on the initial alignment given by a rigid registration stage), but still gives poor results for segmentation. Thus we plan to use it in combination with other segmentation algorithms, for example with deformable models algorithms, in order to delineate more precisely the boundary of the lesions in temporal sequences. At the moment our algorithm has not been specified for multiple sclerosis, but specific processing can be added to the method: shape analysis or even the mean or parametric model of an evolving lesion, or a white matter mask to eliminate false-positives (Warfield et al., 1995). Clinical validation remains to be done, which will require additional work. Then we will compare our results with manual and other automatic segmentation results (Bello and Colchester, 1998). Finally, we plan to apply our approach to study the ‘mass effect’ by quantifying the

evolution of anatomical structures such as the cerebral ventricles or the interface between grey matter and white matter.

Acknowledgements

This work was supported by the EC-funded BIOMORPH project 95-0845, a collaboration between the Universities of Kent and Oxford (UK), ETH Zürich (Switzerland), INRIA Sophia Antipolis (France) and KU Leven (Belgium). Many thanks to Alan Colchester and Fernando Bello (University of Kent at Canterbury) for long discussions about multiple sclerosis and lesions segmentation. We would like to thank Charles Guttmann and Ron Kikinis, Brigham and Women's Hospital, and Harvard Medical School, who provided the multiple sclerosis images time series. Many thanks to Christine Lebrun-Frénay for her help with the validation and for long discussions about multiple sclerosis. We warmly thank Hélène Rastouil for proofreading this paper.

References

Bello, F., Colchester, A., 1998. Measuring global and local spatial correspondence using information theory. In: Wells, W.M., Colchester, A., Delp, S. (Eds.), The First International Conference on Medical Image Computing and Computer-Assisted Intervention, MICCAI'98, Boston. Lecture Notes in Computer Science, Vol. 1496, pp. 964–973.

Bro-Nielsen, M., 1997. Medical image registration and surgery simulation. PhD thesis, IMM (electronic version: http://www.imm.dtu.dk/documents/users/bro/phd.html).

Brown, L.G., 1992. A survey of image registration techniques. ACM Comput. Surv. 24 (4), 325–376.

Cachier, P., Pennec, X., 2000. 3D non-rigid registration by gradient descent on a Gaussian-windowed similarity measure using convolutions. In: Proceedings of the IEEE Workshop on Mathematical Methods in Biomedical Image Analysis (MMBIA'00), Hilton Head Island, SC, pp. 182–189.

Cachier, P., Rey, D., 2000. Symmetrization of the non-rigid registration problem using inversion-invariant energies: application to multiple sclerosis. In: Delp, S.L., DiGioia, A.M., Jaramaz, B. (Eds.), The Third International Conference on Medical Image Computing and Computer-Assisted Intervention, MICCAI'00, Pittsburgh. Lecture Notes in Computer Science, Vol. 1935, pp. 472–481.

Cachier, P., Pennec, X., Ayache, N., 1999. Fast non-rigid matching by gradient descent: study and improvements of the demons algorithm. Technical Report 3706, INRIA (electronic version: http://www.inria.fr/RRRT/RR-3706.html).

Calmon, G., Roberts, N., Eldridge, P., Thirion, J.-P., 1998. Automatic quantification of changes in the volume of brain structures. In: Wells, W.M., Colchester, A., Delp, S. (Eds.), The First International Conference on Medical Image Computing and Computer-Assisted Intervention, MICCAI'98, Boston. Lecture Notes in Computer Science, Vol. 1496, pp. 761–769.

Davatzikos, C., Vaillant, M., Resnick, S., Prince, J.L., Letovsky, S., Bryan, R.N., 1996. Morphological analysis of brain structures using spatial normalization. In: Höhne, K.H., Kikinis, R. (Eds.), Visualization in Biomedical Computing. Lecture Notes in Computer Science, Vol. 1131. Springer, Hamburg, pp. 355–360, electronic version: http://iacl.ece.jhu.edu/_prince/jlp_pubs.html.

Gerig, G., Welti, D., Guttmann, C.R.G., Colchester, A.C.F., Székely, G., 2000. Exploring the discrimination power of the time domain for segmentation and characterization of lesions in serial MR data. Medical Image Analysis 4 (1), 31–42.

Guttmann, C.R.G., Kikinis, R., Anderson, M.C., Jakab, M., Warfield, S.K., Kiliany, R.J., Weiner, H.L., Jolesz, F.A., 1999. Quantitative follow-up of patients with multiple sclerosis using MRI: reproducibility. J. Magn. Reson. Imaging 9, 509–518.

Hajnal, J.V., Saeed, N., Oatridge, A., Williams, E.J., Young, I.R., Bydder, G., 1995. Detection of subtle brain changes using subvoxel registration and subtraction of serial MR images. J. Comput. Assist. Tomogr. 19 (5), 677–691.

Lebrun-Frénay, C., Rey, D., Malandain, G., Chanalet, S., Ayache, N., Chatel, M., 2000. Detection and quantification of MS lesions MRI variations by mathematical differential operators. In: 16th Congress of the European Committee for Treatment and Research in Multiple Sclerosis, Toulouse, France. Revue Neurologique (Supplement), Vol. 156.

Lemieux, L., Wiesmann, U.C., Moran, N.F., Fish, D.R., Shorvon, S.D., 1998. The detection and significance of subtle changes in mixed-signal brain lesions by serial MRI scan matching and spatial normalization. Medical Image Analysis 3 (2), 227–242.

Maes, F., Collignon, A., Vandermeulen, D., Marchal, G., Suetens, P., 1997. Multimodality image registration by maximization of mutual information. IEEE Trans. Med. Imaging 16 (2), 187–198.

Montagnat, J., Delingette, H., 1998. Globally constrained deformable models for 3D object reconstruction. Signal Processing 71, 173–186.

Pennec, X., 1996. L'incertitude dans les problèmes de reconnaissance et de recalage: application en imagerie médicale et biologie moléculaire. PhD Thesis.

Pennec, X., Thirion, J.-P., 1997. A framework for uncertainty and validation of 3D registration methods based on points and frames. Int. J. Comput. Vis. 25 (3), 203–229, electronic version: http://www.inria.fr/epidaure/personnel/pennec/Publications.html.

Prima, S., Thirion, J.-P., Subsol, G., Roberts, N., 1998. Automatic analysis of normal brain dissymmetry of males and females in MR images. In: Wells, W.M., Colchester, A., Delp, S. (Eds.), The First International Conference on Medical Image Computing and Computer-Assisted Intervention, MICCAI'98, Boston. Lecture Notes in Computer Science, Vol. 1496, pp. 770–779.

Rey, D., Subsol, G., Delingette, H., Ayache, N., 1998. Automatic detection and segmentation of evolving processes in 3D medical images: application to multiple sclerosis. Technical Report 3559, INRIA (electronic version: http://www.inria.fr/RRRT/RR-3559.html).

Rey, D., Delingette, H., Subsol, G., Ayache, N., 1999. Using continuum mechanics operators for detection and quantification of evolving processes in 3D medical images. In: EUROMECH406, Warsaw, Poland, pp. 185–188, electronic version (abstract): http://at.yorku.ca/cgi-bin/amca/cacp-11.

Rey, D., Lebrun-Frénay, C., Malandain, G., Chanalet, S., Ayache, N., Chatel, M., 2000. A new method to detect and quantify evolving MS lesions by mathematical operators. Neurology (Supplement) 54 (7), 123.

Roche, A., Malandain, G., Ayache, N., 2000. Unifying maximum likelihood approaches in medical image registration. Int. J. Imaging Syst. Technol. 11, 71–80.

Thirion, J.-P., 1996. New feature points based on geometric invariants for 3D image registration. Int. J. Comput. Vis. 18 (2), 121–137; electronic version: http://www.inria.fr/RRRT/RR-1901.html.

Thirion, J.-P., 1998. Image matching as a diffusion process: an analogy with Maxwell's demons. Medical Image Analysis 2 (3), 243–260; electronic version: http://www.inria.fr/RRRT/RR-2547.html.

Thirion, J.-P., Calmon, G., 1999. Deformation analysis to detect and quantify active lesions in 3D medical image sequences. IEEE Trans. Med. Imaging 18 (5), 429–441; electronic version: http://www.inria.fr/RRRT/RR-3101.html.

Warfield, S., Dengler, J., Zaers, J., Guttmann, C.R.G., Wells, W.M., Ettinger, G.J., Hiller, J., Kikinis, R., 1995. Automatic identification of grey matter structure from MRI to improve the segmentation of white matter lesions. J. Image Guided Surg. 1 (6), 326–338.

Weiss, J.A., Maker, B.N., Govindjee, S., 1997. Finite element implementation of incompressible transversely isotropic hyperelasticity. Comput. Methods Appl. Mech. Eng. 135, 107–128.

Welti, D., Gerig, G., Radü, E.-W., Kappos, L., Székely, G., 2001. Spatio-temporal segmentation of active multiple sclerosis lesions in serial MRI data. In: Insana, M.F., Leahy, R.M. (Eds.), 17th International Conference on Information Processing in Medical Imaging (IPMI'01), Davis, CA. Lecture Notes in Computer Science, Vol. 2082, pp. 438–445.

Zijdenbos, A., Forghani, R., Evans, A., 1998. Automatic quantification of MS lesions in 3D MRI brain data sets: validation of insect. In: Wells, W.M., Colchester, A., Delp, S. (Eds.), The First International Conference on Medical Image Computing and Computer-Assisted Intervention, MICCAI'98, Boston. Lecture Notes in Computer Science, Vol. 1496, pp. 439–448.